Article

Enhanced Adsorption−Photocatalytic Degradation of Organic Pollutants *via* a ZIF-67-Derived Co−N Codoped Carbon Matrix Catalyst

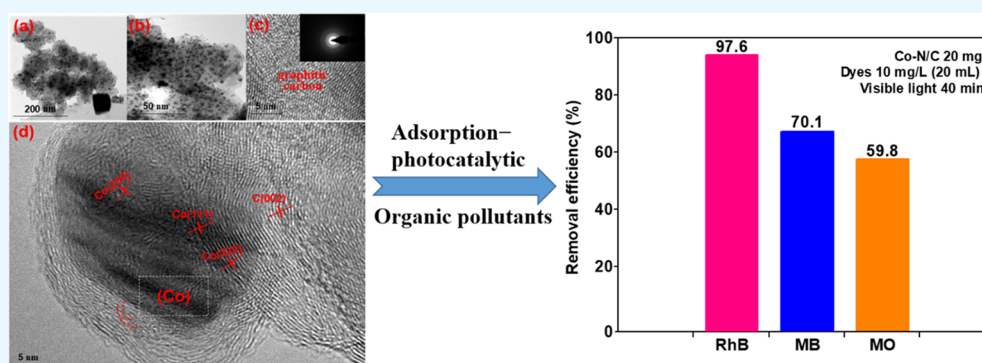Zheng Yang,* Heng-Shen Xie,* Wei-Yuan Lin, Yi-Wu Chen, Daoguang Teng,* and Xing-Shun Cong

Read Online

ACCESS | Metrics & More | Article Recommendations | SI Supporting Information

ABSTRACT: Stable and efficient photocatalytic degradation of organic pollutants has been achieved *via* a ZIF-67-derived Co-embedded N-doped nanoporous carbon material catalyst (Co−N/C). The catalyst features a well-distributed structure, suitable specific surface area, and more active sites according to the various characterization analyses. The photocatalytic activity of Co−N/C was evaluated by the degradation of the target pollutant Rhodamine B (RhB). As a result, RhB could establish an adsorption−desorption equilibrium in the dark within 30 min and was thoroughly degraded into H_2O and CO_2 by Co−N/C under 500 W visible light irradiation in 40 min. Moreover, radical-quenching experiments and reactive oxygen species monitoring were performed to further probe the plausible photodegradation mechanism of RhB. Co−N/C is also appropriate for other alternative dyes and antibiotics affording ideal removal efficiencies. After the reaction, Co−N/C could be facilely separated by an external magnetic field and reused for eight reaction cycles without obvious deactivation of its photocatalytic properties. This study is expected to provide an instructive guideline for the design of efficient and recyclable composite photocatalysts derived from metal−organic frameworks for a broad range of environmental remediation processes.

1. INTRODUCTION

With the rapid development of global industrialization, water pollution is becoming increasingly serious and creating significant problems for microorganisms and human society.[1,2] Organic dyes and heavy metal ions are considered as the most carcinogenic and toxic pollutants in wastewater because they directly threaten the water source quality and damage the ecological balance.[3−5] For the past several decades, many techniques have been widely proposed for treating organic wastewater, such as carbon adsorption, advanced oxidation, membrane technology, and biological decomposition.[6−9] Among these, the adsorption method is currently recognized as a simple, economical, and practical technology to adsorb and remove wastewater pollutants. However, the regeneration/ low efficiency of some adsorbents and the complex composition of industrial wastewater are still a problem. Therefore, there is an urgent demand to probe more advanced protocols combined with adsorption techniques for eliminating

organic pollutants (OPs) from wastewater in both scientific and industrial fields.

Photocatalysis has been overwhelmingly utilized in the removal of OPs from wastewater because of its high efficiency, low cost, and absence of secondary pollutants.[10] A survey of the literature shows that semiconductor photocatalysts, such as TiO_2, ZnO, CdS, and g-C_3N_4,[11−14] were efficiently developed for OP degradation, in which the main products are less toxic organic molecules and inorganic CO_2, H_2O (NO_3^-, PO_4^-), and halide ions.[15] Moreover, the few surface active sites, easy agglomeration, and low solar energy utilization efficiency of

some inorganic catalysts restrict their large-scale practical applications. Significantly, photocorrosion is a typical disadvantage of photocatalysis, and semiconductor photocatalysts are usually unstable under the operating conditions. The catalyst corrosion caused by light illumination in aqueous media contributes to the migration of metal ions and the dissolution of solid photocatalysts.[16,17] Carbon matrix materials generally have high conductivity and good chemical stability.[18,19] Improved carbon-based materials for building composite catalysts could effectively promote the charge transfer and extend.[20,21] Thus, the exploitation of appropriate photocatalytic materials with stability and high performance to remove OPs in water has been attracting great attention.

Metal−organic frameworks (MOFs) have emerged as prospective precursors to manufacture nonprecious materials due to the flexible porous properties, controllable composition, and high carbon/nitrogen content.[22−25] In particular, MOFs show prospects in versatile applications, including adsorption, photocatalysis, separation, gas storage, electrochemistry, and fluorescence.[26−30] Recently, MOFs have been utilized as templates to prepare nanoporous carbons, which exhibit a large surface area and high electrochemical performance.[31,32] The metal ions could be encapsulated in ligand-derived carbon layers without obvious agglomeration by carbonization of the MOF precursors containing the metal centers.[33−35] The synergistic effect of carbon materials and metals could accelerate the reactions and inhibit electron−hole recombination, which could tackle the bottlenecks for the conventional photocatalytic removal of OPs.[36,37] For instance, Guo and co-workers developed the Co_3O_4/C catalyst by calcining activated carbon-modified MOF precursors for the decolorization of methylene blue (MB) under UV−visible light.[38] Park et al. prepared ZnO/C hybrids by the carbonization of MOF-5 and the obtained composite materials exhibited photocatalytic degradation on Rhodamine B (RhB).[39] Similarly, Xia et al. exploited N-doped ZnO nanoporous carbon composites derived from ZIF-8 for CO_2 uptake and MB removal from water.[40,41] With these in mind, the development of a high-performance and excellent stability photocatalyst based on MOF-derived nanoporous carbon materials is strongly desired for the degradation of OPs in wastewater.

Herein, a Co-encapsulated N-doped nanoporous carbon material was synthesized by a facile strategy (denoted as Co−N/C). The efficient and recyclable Co−N/C was prepared through pyrolysis carbonization of the ZIF-67 parent, and then, the catalyst was applied to the degradation of OPs. The degradation efficiency of RhB reaches 97.6% in a short time using Co−N/C with high stability and reusability. In addition, our results showed that the prepared Co−N/C could achieve efficient degradation of dyes and antibiotics under visible light irradiation. We further examined the reusability and regeneration of Co−N/C eight times. A feasible photocatalytic mechanism of Co−N/C was proposed via radical quenching experiments and electron paramagnetic resonance (EPR) technique.

2. EXPERIMENTAL SECTION

2.1. Materials. RhB, MB, methyl orange (MO), tetracycline hydrochloride (TCHC), norfloxacin, isopropanol (IPA), 1,4-benzoquinone (BQ), and ethylenediaminetetraacetic acid disodium salt (EDTA-2Na) were purchased from Energy Chemical Industrial Inc., Shanghai, China, and used as received. 2-Methylimidazole (98%) and cobalt nitrate (Co-

$(NO_3)_2 \cdot 6H_2O$, >99%) were purchased from Sinopharm Chemical Reagent Co., Ltd., Shanghai, China. Solvents ethanol and methanol were obtained from commercial sources and purified by distillation before use.

2.2. Catalyst Preparation. The ZIF-67 precursor was prepared with some modifications according to procedures in the previous literature.[42] To a 50 mL Schlenk tube under air atmosphere, $Co(NO_3)_2 \cdot 6H_2O$ (1.55 mmol), 2-methylimidazole (67 mmol), and ethanol (50 mL) were successively added and stirred at 50 °C for 4 h. Then, the resulting residue was purified by recrystallization and washed with ethanol (3 × 25 mL) to afford the desired product as purple precipitates.

Co−N/C was obtained by carbonization of the ZIF-67 parent. Typically, ZIF-67 (2.0 g) was carbonized at different set temperatures for 5 h and then annealed to prepare the Co nanoparticle catalyst, denoted as Co−N/C(T), where T indicates the thermolysis temperature of the ZIF-67 MOFs (T = 600, 700, and 800 °C).

2.3. Characterization Techniques of Materials. Element compositions were determined by an ESCA LAB MK-II X-ray photoelectron spectrometer (XPS, Al Kα radiation). A Bruker AXS D8 ADVANCE diffractometer was used to characterize the powder X-ray diffraction (XRD) patterns (Cu Kα source, λ = 1.5406 Å). Microscopic images were investigated by scanning electron microscopy (SEM, Hitachi S-3700 N) and transmission electron microscopy (TEM, JEM-2100, 200 kV). Specific surface areas were determined via a Micromeritics analyzer at 77 K using the Brunauer−Emmett−Teller (BET) method (Autosotrb-IQ2-MP-XR).

2.4. Pollutant Adsorption and Photocatalytic Degradation. RhB was utilized as a model pollutant to probe the adsorption of the ZIF-67 precursor and Co−N/C. The adsorption performance was evaluated by dispersing 20 mg of the material in 20 mL of RhB (10 mg/L) solution with stirring in the dark at room temperature until the adsorption and desorption equilibrium was achieved. About 3 mL aliquots were sampled at certain intervals, and the solid was removed by a filter membrane (0.45 μm).

Removal efficiency (R) of RhB was calculated by eq 1

$$R = \frac{c_0 - c_t}{c_0} \times 100\% \tag{1}$$

where C_0 and C_t are the concentrations of RhB at contact times of 0 and t, respectively.

The reaction kinetic study was investigated by the pseudo-first-order model eq 2.

$$-\ln(C_t/C_0) = k \cdot t \tag{2}$$

where k is the apparent rate constant of the equation.

The photocatalytic degradation performances of materials were determined using RhB solution with a 500 W Xe lamp (λ > 420 nm). Typically, a certain amount of Co−N/C was added into 20 mL of RhB solution (10 mg/L) and then stirred for 30 min in the dark. Then, after irradiation for an appropriate time interval, fixed amounts of the reaction system were taken out from the reactor and filtered by a 0.45 μm filter membrane for further analysis. In addition, the effects of the photocatalyst dosage (4, 8, 12, 16, and 20 mg), photocatalytic degradation time (8, 16, 24, 32, and 40 min), and target pollutants (RhB, MB, MO, and TC) on the photodegradation performance were thoroughly researched. The concentrations of RhB, MB, MO, and TC in the solutions could be determined via UV−vis
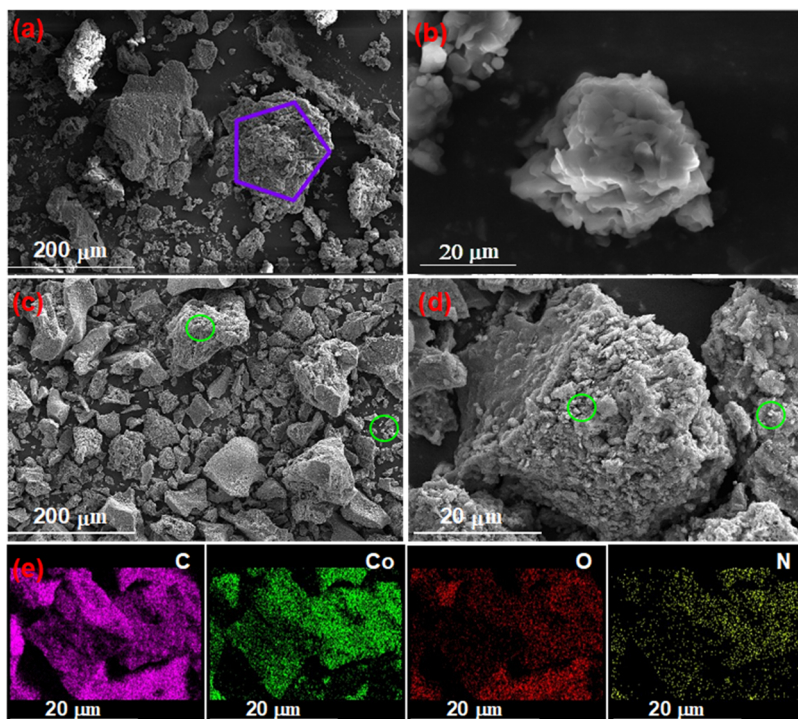
Figure 1. (a, b) SEM images of ZIF-67; (c, d) SEM images of Co−N/C; (e) corresponding element mapping images of C, Co, O, and N for Co−N/C.
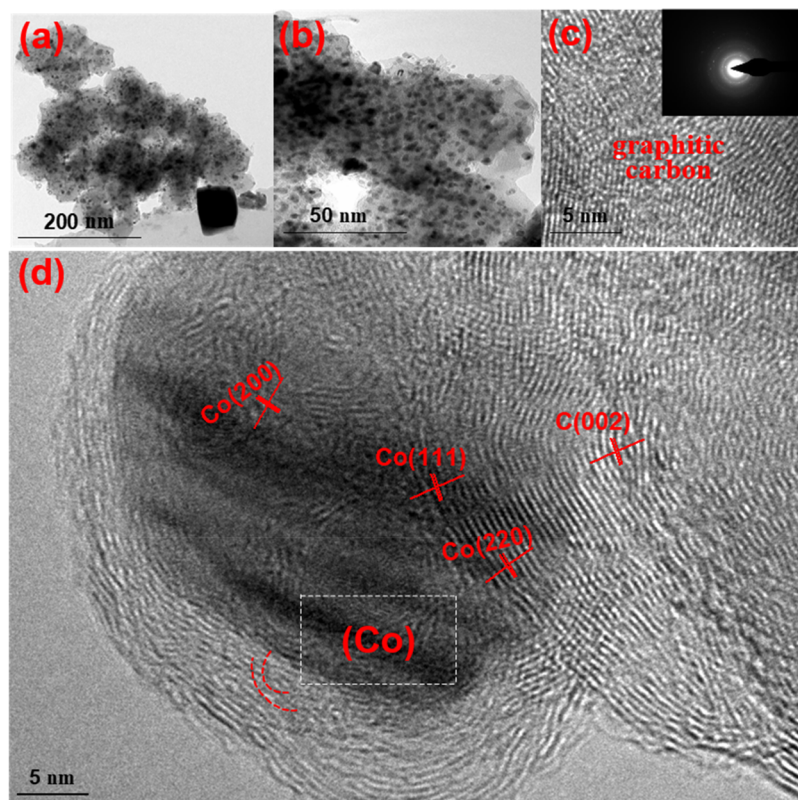

**Figure 2.** (a−d) TEM images of Co−N/C; inset: SEAD pattern of Co−N/C.

spectroscopy, and the R of the target pollutants was calculated according to eq 1.

To demonstrate the reactive species involved in the photocatalytic reaction, IPA (2 mL), EDTA-2Na (1.0 equiv), and BQ (1.0 equiv) were used in photocatalytic experiments.

Co−N/C was recycled and washed with methanol thoroughly and dried at 60 °C for 12 h. The collected photocatalyst was used for the cycle experiment of RhB degradation under the same conditions.
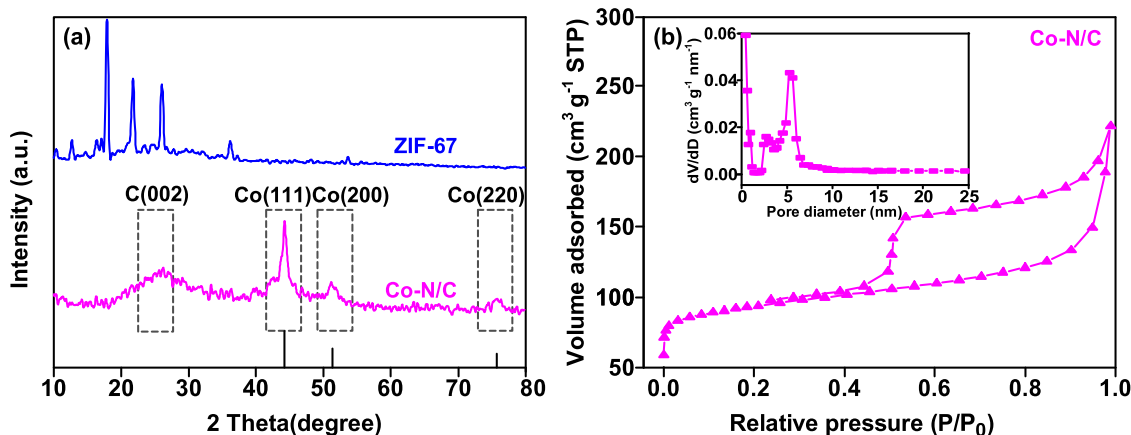
Figure 3. (a) XRD patterns of ZIF-67 and Co−N/C; (b) N_2 adsorption/desorption isotherms of Co−N/C; the inset image displays the pore size distribution curve.
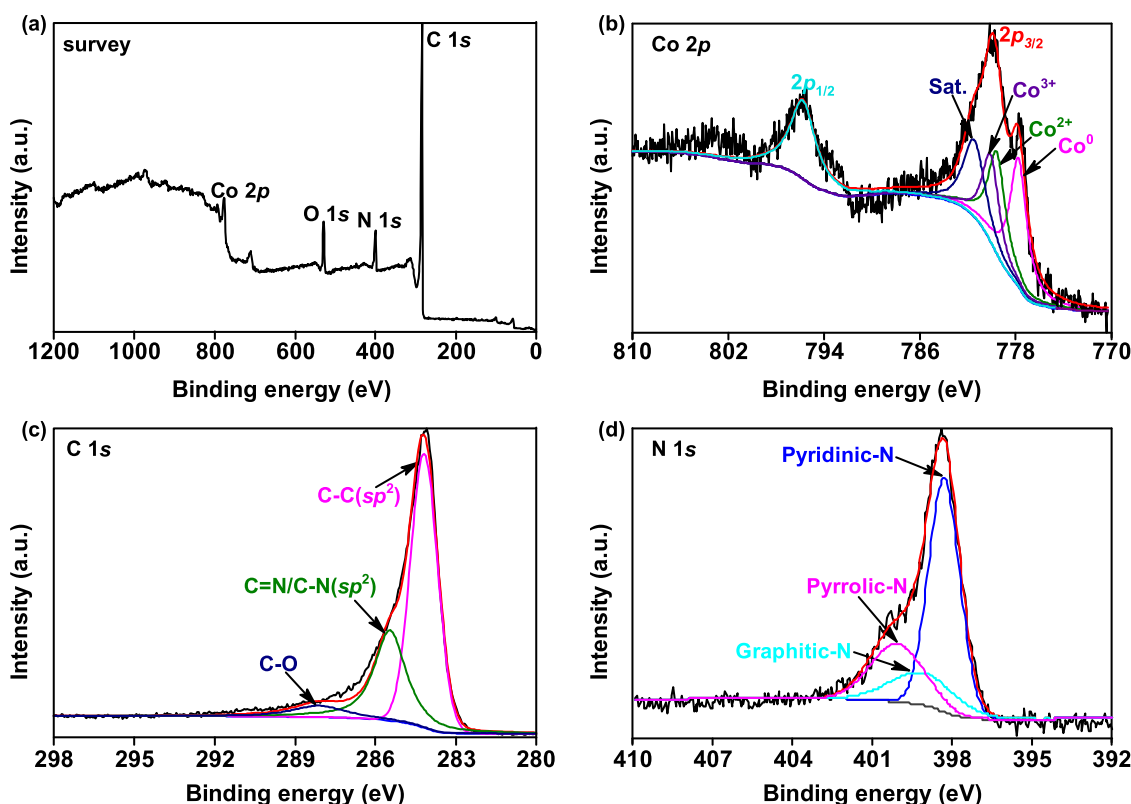

Figure 4. (a) XPS of Co−N/C; (b) high-resolution Co $2p$ spectra of Co−N/C; (c) high-resolution C $1s$ spectra of Co−N/C; (d) high-resolution N $1s$ spectra of Co−N/C.

3. RESULTS AND DISCUSSION

3.1. Characterization of the Prepared Materials. The scanning electron microscopy (SEM) (Figure 1a,b) image clearly exhibits a polyhedral structure and morphology of the synthesized ZIF-67 with a well-defined crystal shape and smooth surface. More importantly, the slightly rougher surface and relatively smaller particles on the surface of Co−N/C can be observed, indicating the gradual carbonization of ZIF-67 (zeolitic imidazolate framework) (Figure 1c,d). During the thermolysis procedure, most cobalt oxide species were reduced to Co^0 with the carbonization of 2-methylimidazole in ZIF-67.[43] Interestingly, the N-doped carbon matrix materials presented a prominent property in embedding the Co species,

resulting in high dispersion characteristics without apparent agglomeration. The mapping image observations showed the homogeneous distribution of C, N, O, and Co elements on the Co−N/C surface. In addition, the contents of C, N, and Co were found to be *ca.* 60.3, 10.2, and 17.3 wt %, respectively, by energy-dispersive X-ray analysis (Figure S1).

The morphology of Co−N/C was further characterized by transmission electron microscopy (TEM). As shown in Figure 2a,b, some favorably dispersed black nanoparticles were located on the surface of Co−N/C. Figure 2c further shows a typical TEM image of the edge of Co−N/C, where the Co nanoparticles are entirely encapsulated by the carbon matrix. Figure 2d indicates the existence of crystalline Co NPs with crystal lattice spacing. The selected area electron diffraction
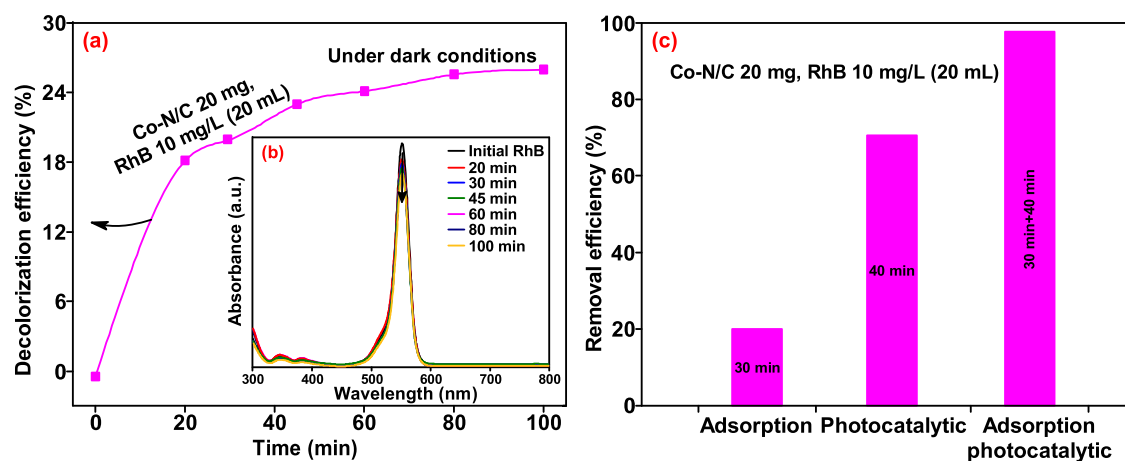
Figure 5. (a) Effect of contact time on the RhB decolorization efficiency by Co−N/C in the dark. (b) Temporal UV−vis absorption spectra of RhB in the presence of Co−N/C in the dark. (c) Removal efficiency of RhB over Co−N/C under different conditions.

Table 1. Photocatalytic performance of various materials for the degradation of RhB[a]

	removal efficiency (%)						
catalyst	−30 min	0 min	8 min	16 min	24 min	32 min	40 min
ZIF-67	25.8	25.8	26.2	26.7	27.4	27.6	28.6
Co−N/C (600)	20.1	20.1	48.1	62.7	76.9	92.0	97.6
Co−N/C (700)	18.3	18.3	42.3	50.9	58.3	63.7	65.2
Co−N/C (800)	14.3	14.3	38.7	46.6	53.4	58.6	62.5

[a]Reaction conditions: RhB 10 mg/L (20 mL), material (20 mg), adsorption time (30 min), and photocatalysis (0−40 min).

pattern of the Co−N/C nanoparticle verifies its polycrystalline structure (inset).

The XRD patterns of the synthesized ZIF-67 and Co−N/C are illustrated in Figure 3a. Apparently, the peak observed at about 26.0° corresponds to the (002) plane of carbon (graphitic carbon). Other characteristic diffraction peaks of the lattice planes from Co−N/C at 44.2° (111), 51.6° (200), and 76.0° (220), respectively, are attributed to the metal Co, indicating that the ZIF-67 precursor could convert into Co-based materials by pyrolysis at high temperatures.[43,44]

As Figure 3b presents, the distribution curve of Co−N/C shows typical type IV adsorption and desorption isotherms with a hysteresis loop, suggesting the existence of a micro-/mesoporous structure. According to the BET method, the surface area of Co−N/C was calculated as 379.32 m²/g (Table S3). The micro-/mesoporous structure and higher specific surface area are in favor of exposing more active sites and improve the efficiency of adsorption−photocatalytic reaction.[45]

The high-resolution XPS spectral analysis confirmed the coexistence of Co 2p, C 1s, N 1s, and O 1s in Co−N/C (Figure 4a). In addition, the atomic densities of C, N, and Co are ca. 75.93, 9.56, and 4.80 atom %, respectively (Table S1), which coincide with the EDX patterns. As shown in Figure 4b, the two high-resolution peaks of Co 2p at 781.3 and 796.0 eV could be attributed to Co $2p_{3/2}$ and Co $2p_{1/2}$, respectively.[46] Obviously, the Co $2p_{3/2}$ regions consisted of three contributions at 778.8, 780.2, and 781.9 eV, which belong to metallic Co, Co^{2+}, and Co^{3+} (cobalt oxides), respectively.[47] The Co^{2+} and Co^{3+} species could originate from the surface oxidation of metallic Co. Among carbon regions, three characteristic peaks appeared at 286.8, 285.7, and 284.7 eV, which correspond to the C−O bonds, C=N/C−N (sp²), and C−C (sp²) bonds (Figure 4c),[48] respectively. For the high-resolution N 1s spectra in Figure 4d, the sample displayed three typical types of

nitrogen species, attributed to the pyridinic-N (398.4 eV), pyrrolic-N (399.6 eV), and graphitic-N (401.2 eV),[49,50] which further indicated that the N atom was doped successfully. Previous studies show that N-doping influences the electronic/chemical properties and accelerates the photochemical performances of carbon materials.[51] In addition, higher contents of pyridinic-N and/or pyrrolic-N in the Co−N/C material promote the electron-transfer efficiency.[52]

3.2. RhB Adsorption Experiments. Absorption experiments for RhB were explored to determine the adsorption capacity of Co−N/C. Figure 5a,b displays the UV−vis absorbance spectra of RhB under dark conditions using Co−N/C. Obviously, Co−N/C showed a comparatively superior adsorption capacity of RhB in the first 20 min, and an adsorption−desorption equilibrium was gradually achieved afterward. The adsorption quantity of RhB increased only slightly on prolonging the reaction time from 30 (20.1%) to 100 min (26.0%). In addition, compared with direct visible-light irradiation, adsorption photocatalysis possessed a higher removal efficiency, which was ascribed to the larger specific surface area, and the special composition of Co−N/C improved the photocatalytic effect (Figure 5c).

3.3. Photocatalytic Degradation of RhB with Various Materials. As summarized in Table 1, catalytic activities of various materials were probed for the photocatalytic degradation of RhB for 40 min. Apparently, the ZIF-67 precursor afforded the lowest photocatalytic performance and exhibited the maximum adsorption capacity (in darkness for 30 min), which was attributed to the ultrahigh surface area (Table S2). Co−N/C derived from ZIF-67 showed good activity in this photocatalytic system, and Co−N/C carbonized at 600 °C presented excellent catalytic activity, affording 97.6% removal efficiency. However, the Co−N/C (700) material with the largest RhB adsorption did not exhibit the desired removal
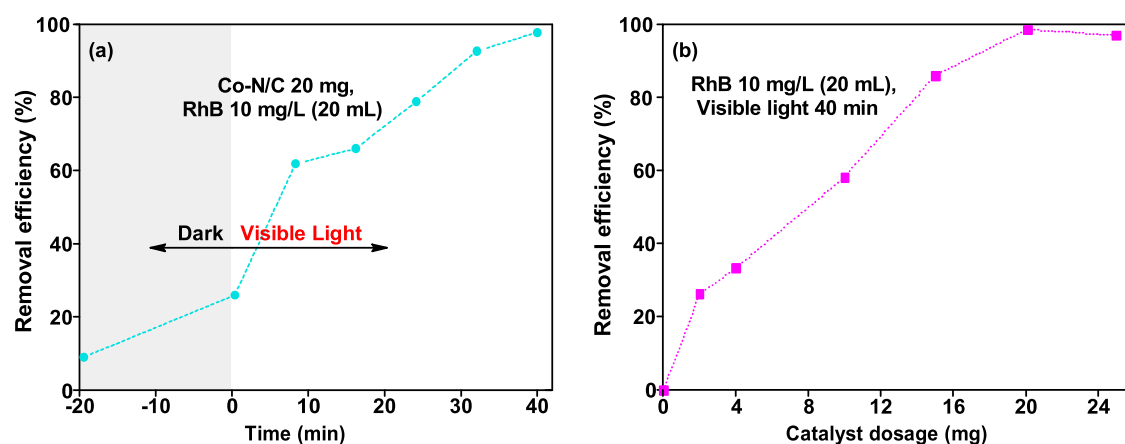
Figure 6. Effects of (a) contact time and (b) catalyst dosage on the RhB removal efficiency.
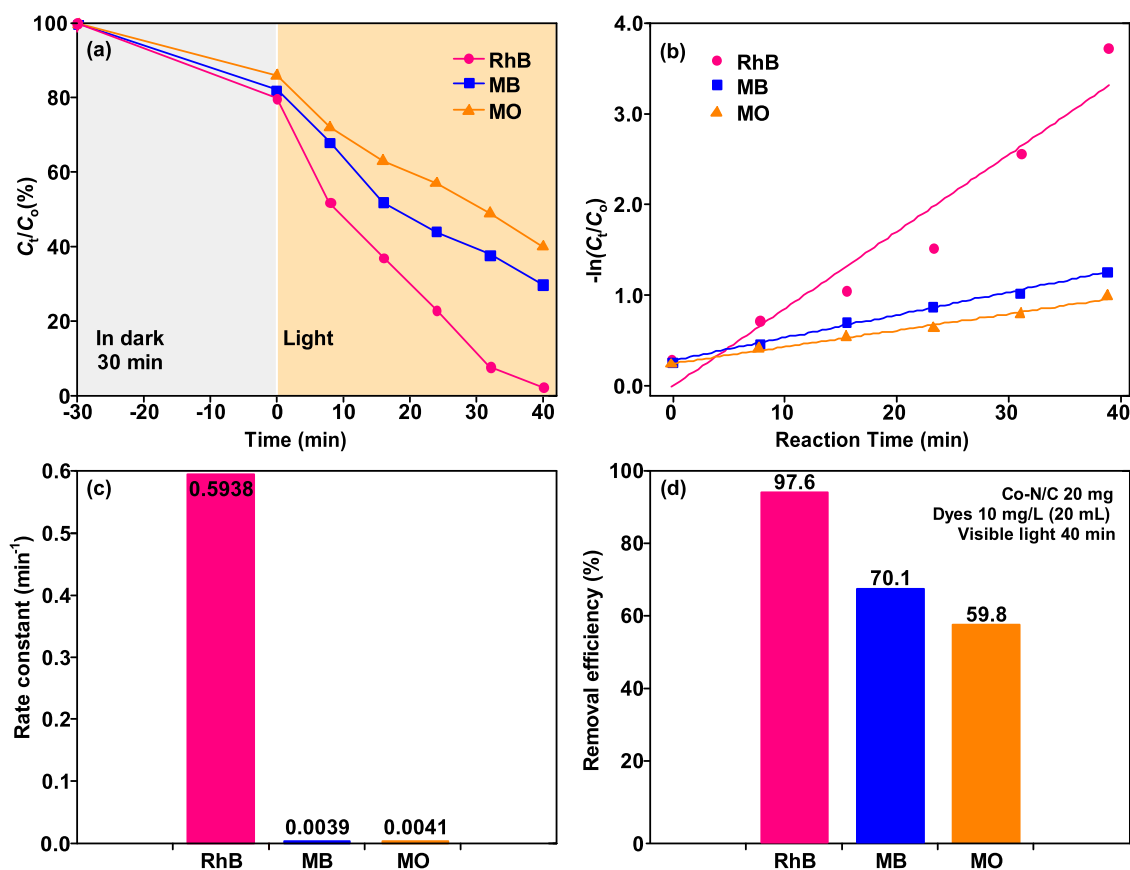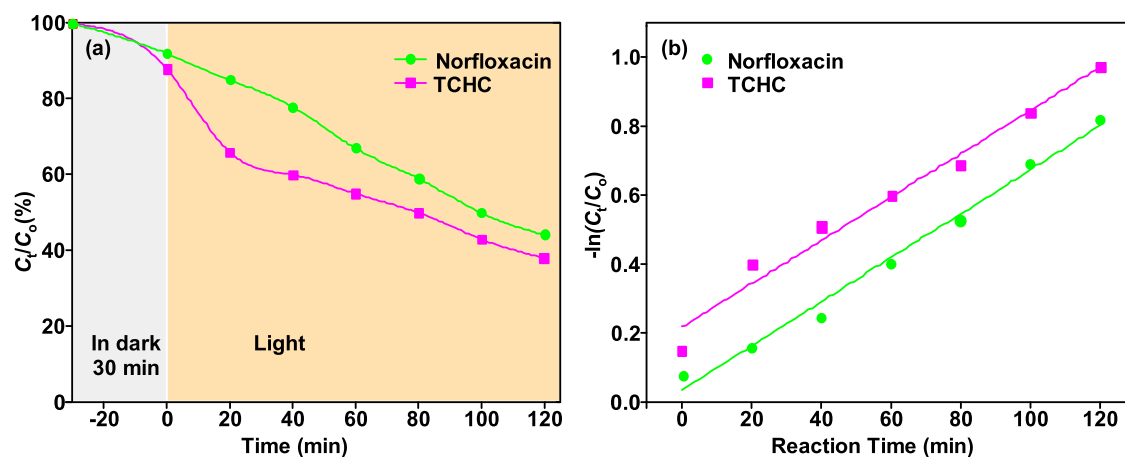

Figure 7. Photocatalytic degradation performances of Co−N/C: (a) total photocatalytic degradation curves of RhB, MB, and MO; (b) linear fitting of the pseudo-first-order kinetic equation; (c) histogram of the apparent rate constant; (d) effect of the dye type on the removal efficiency under the same conditions.

efficiency. The result further indicates that specific surface areas and adsorption abilities are beneficial to RhB photodegradation but not a decisive factor in this system. Co NP crystal aggregation and particle size were increased at higher calcination temperatures (700 and 800 °C). A small particle size could increase surface-active catalytic sites to some extent and then promote photocatalytic RhB degradation.

3.4. Degradation of RhB under Different Conditions. Optimization of the photocatalytic reaction conditions was performed by taking Co−N/C and RhB as the model substrates. Obviously, RhB could not degrade within 40 min when no catalyst was added, indicating that the self-photolysis

of RhB was negligible. Figure 6 summarizes the photodegradation results of RhB under different conditions after the adsorption equilibrium. The optimal contact time for the photocatalytic degradation of RhB was investigated in the range of 0−40 min. After only 8 min, *ca.* 48.1% RhB could be effectively removed. It turned out that the photocatalytic degradation reaction could proceed in a short time in the presence of Co−N/C. The removal of RhB can be intuitively determined by the color change of the reaction system. The maximum RhB removal efficiency attained was around 97.6% for 40 min. In addition, we further examined the impact of the catalyst dosage on reaction activities. Specifically, the RhB

Figure 8. Photocatalytic degradation performances of Co−N/C: (a) total photocatalytic degradation curves of norfloxacin and TCHC; (b) linear fitting of the pseudo-first-order kinetic equation.
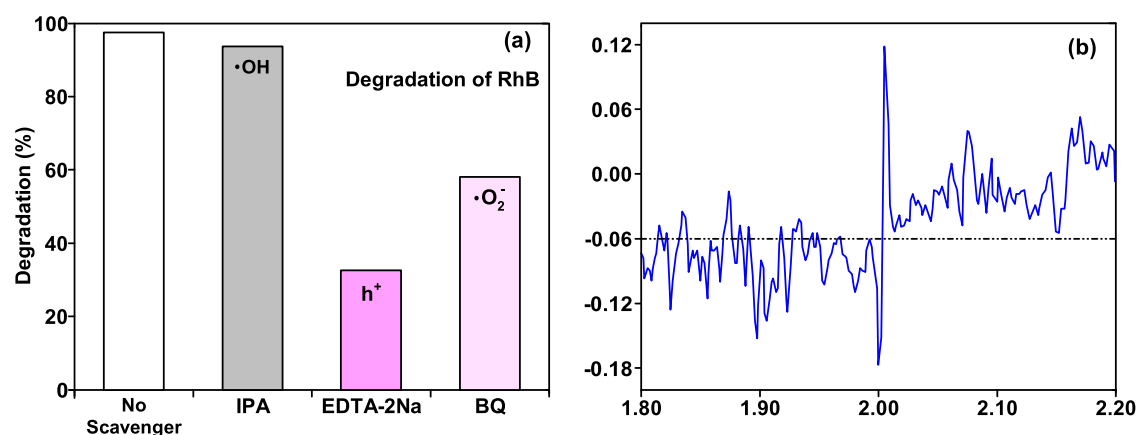
Figure 9. (a) Effect of different scavengers on the degradation of RhB over Co−N/C in water under visible light irradiation for 40 min; (b) electron paramagnetic resonance of Co−N/C.

removal efficiency substantially increased as the Co−N/C amount increased from 2 to 20 mg and reached maximum efficiency. On further increasing the Co−N/C feed to 25 mg, the removal efficiency of RhB slightly decreased, which could be ascribed to the limitations of mass transfer and/or the light-shielding effect caused by the excessive catalysts.[10]

3.5. Photocatalytic Degradation of Other Organic Pollutants. The universality and scope of the photocatalytic activities of the prepared Co−N/C were further probed by degrading other alternative organic pollutants (MB, MO, TCHC, and norfloxacin) under similar conditions. As Figure 7a shows, 13.8 and 17.9% of the initial MB and MO are degraded, respectively, in the dark within 30 min, which indicated that the self-degradation efficiency of dyes is still not sufficient, and the enhancement of the photoexcited catalyst is essential. Interestingly, after only 16 min under irradiation, *ca.* 62.7% RhB, 47.7% MB, and 36.9% MO could be effectively degraded. This further confirmed the high catalytic activities and strong light-harvesting capacities of the photocatalyst. As presented in Figure 7d, 97.6 of RhB was removed in the presence of Co−N/C and about 70.1 and 59.8% of MB and MO, respectively, were degraded at the irradiation time of 40 min (Figure 7d). In addition, Figure 7b shows the pseudo-first-order kinetic model of organic dye photodegradation. Obviously, the degradation of RhB exhibited the steepest straight line with the largest slope value among the three dyes

by linear fitting, which indicates fast photocatalytic degradation on the photocatalyst. The apparent rate constant k of the kinetic equation is summarized in Figure 7c. The highest k value is achieved on RhB (0.5938 min^{-1}), followed by MB (0.0041 min^{-1}) and MO (0.0039 min^{-1}).

Furthermore, TCHC and norfloxacin were also used as the target pollutants to demonstrate the selectivity of Co−N/C. As indicated in Figure 8a, both 13.8% of the initial TCHC and 8.0% of the initial norfloxacin are degraded under dark conditions for 30 min in the presence of Co−N/C, indicating that TCHC is less stable than norfloxacin. After 120 min irradiation, the total removal efficiencies of TCHC and norfloxacin reached *ca.* 61.8 and 55.7%, respectively. Meanwhile, the reaction kinetics for degradations of TCHC and norfloxacin over Co−N/C were studied, and the results are depicted in Figure 8b. The result accords with the pseudo-first-order kinetics, the rate of which could be acquired from the slope of the reaction plot. As expected, the photodegradation of TCHC achieved a higher k value of 0.0105 min^{-1} over the Co−N/C system, which was almost 2.2 times higher than that of norfloxacin (0.0049 min^{-1}). The high removal rates of organic pollutants (RhB, MB, MO, TCHC, and norfloxacin) demonstrated the availability of the Co−N/C photocatalyst.

3.6. Plausible Reaction Pathway of RhB Degradation. To understand the main mechanism of the photocatalytic degradation of RhB, the effect of several reactive scavenger

species on the photocatalytic properties was determined. Specifically, IPA, EDTA-2Na, and BQ were used as ●OH, h$^+$ and ●O$_2^-$ scavengers,[53] respectively. As presented in Figure 9a, RhB can be almost completely removed without the addition of any scavengers. Meanwhile, it was found that the ●OH radical is not the main active species and made a minor contribution to the RhB removal efficiency as the presence of IPA caused only a slight decrease. Noteworthily, the removal efficiency of RhB was reduced to 44.7 and 64.2% after the introduction of radical scavengers EDTA-2Na and BQ, respectively, which further demonstrated that ●O$_2^-$ and h$^+$ dominated the photocatalytic degradation process. In addition, the electron paramagnetic resonance technique was used to monitor the oxygen vacancies (active specie) of Co−N/C, which could further facilitate the separation of photogenerated carriers (Figure 9b).

With the above experimental results, a plausible photocatalytic degradation mechanism of RhB with Co−N/C was put forward (Figure 10). In the presence of visible light, the
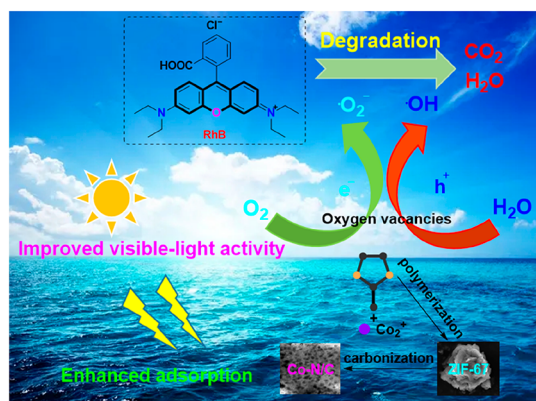
Figure 10. Plausible RhB photocatalytic degradation mechanism with Co−N/C under visible light irradiation.

photogenerated electrons are transferred to the adsorbed O$_2$ on the Co−N/C surface to produce ●O$_2^-$. Subsequently, the resulting ●O$_2^-$ and h$^+$ could further degrade RhB to form small-molecule compounds (CO$_2$ and H$_2$O).

3.7. Reusability of Co−N/C for the Photocatalytic Degradation of RhB. The recyclability and stability of the Co−N/C photocatalyst were probed under optimum con-

ditions. Co−N/C could be recycled by an external magnetic field from the reaction solution after the reaction due to its good magnetic properties. As Figure 11 exhibits, the degradation efficiency presents no apparent decrease after recycling eight times. More than 95% of the RhB removal efficiency is maintained in the whole recycling reaction, which suggested that the good photocatalytic performance of Co−N/C could be maintained over a longer time period. Furthermore, the XRD pattern analysis shows that the peak intensity and position of Co−N/C showed almost no shift, indicating its outstanding structural stability in eight reaction cycles (Figure S2a). The transmission electron microscopic image of the reused catalyst shows that there was almost no severe agglomeration of the Co nanoparticles on the Co−N/C surface, which could be ascribed to the stabilized structure derived from ZIF-67 MOFs and the highly dispersed Co nanoparticles (Figure S2b). The above results further demonstrate the stability and potential application of the prepared Co−N/C photocatalyst in industrial fields.

4. CONCLUSIONS

In this study, Co−N codoped nanoporous carbon materials (Co−N/C) are obtained *via* a facile carbonization method using ZIF-67 as the precursor. The outstanding adsorption−photocatalytic performance toward Co−N/C is ascribed to its suitable specific surface area, well-distributed structure, and efficient transportation of photogenerated carriers. Notably, Co−N/C featured an excellent degradation rate for RhB upon 40 min visible-light irradiation. Radical quenching experiments and reactive oxygen species monitoring confirmed that h$^+$ (●O$_2^-$) and oxygen vacancies dominated the photocatalytic degradation process of RhB. Co−N/C was also available for the degradation of other OPs such as MB, MO, TCHC, and norfloxacin. Moreover, the catalyst shows good stability for eight reaction cycles without obvious deactivation. This study provides a simple strategy for the fabrication of the doped porous carbon materials for enhancing the adsorption−photocatalytic degradation of contaminants in wastewater.

■ ASSOCIATED CONTENT

Ⓢ Supporting Information

The Supporting Information is available free of charge at https://pubs.acs.org/doi/10.1021/acsomega.2c03846.
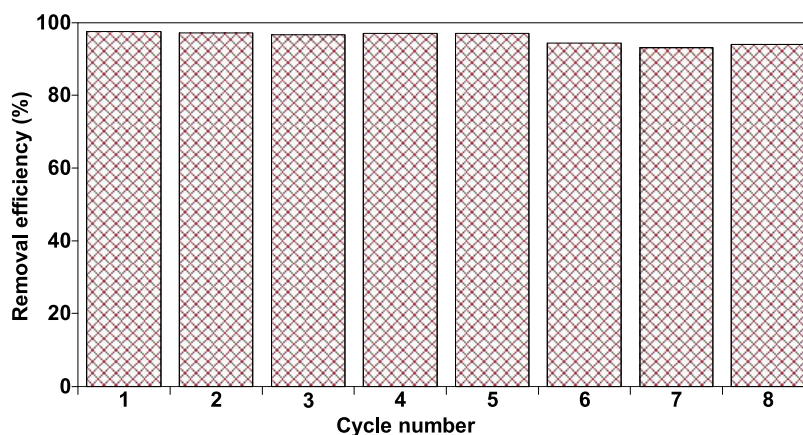
Figure 11. RhB concentration changes in eight reaction cycles under Co−N/C (initial concentration of RhB = 10 mg/L, irradiation time = 40 min).

Physical and chemical nature of materials (ZIF-67 and Co−N/C) (Figures S1 and S2, Tables S1 and S3), and pore texture parameters of Co−N/C (Table S2) (PDF)

AUTHOR INFORMATION

Corresponding Authors

Zheng Yang − School of Architectural Intelligence, Jiangsu Vocational Institute of Architectural Technology, Xuzhou 221116, P. R. China; Jiangsu Collaborative Innovation Center for Building Energy Saving and Construct Technology, Xuzhou 221116, P. R. China; Jiangsu Engineering Laboratory of Biomass Resources Comprehensive Utilization, Jiangsu Vocational Institute of Architectural Technology, Xuzhou 221116, P. R. China; College of Chemical Engineering, Zaozhuang University, Zaozhuang 277160, P. R. China; orcid.org/0000-0001-6504-9145; Email: yang_chem@126.com

Heng-Shen Xie − Jiangsu Engineering Laboratory of Biomass Resources Comprehensive Utilization, Jiangsu Vocational Institute of Architectural Technology, Xuzhou 221116, P. R. China; Email: hkxie_xz@163.com

Daoguang Teng − School of Chemical Engineering, Zhengzhou University, Zhengzhou 450001, P. R. China; orcid.org/0000-0001-9120-3070; Email: teng_daoguang@zzu.edu.cn

Authors

Wei-Yuan Lin − School of Architectural Intelligence, Jiangsu Vocational Institute of Architectural Technology, Xuzhou 221116, P. R. China; Jiangsu Engineering Laboratory of Biomass Resources Comprehensive Utilization, Jiangsu Vocational Institute of Architectural Technology, Xuzhou 221116, P. R. China

Yi-Wu Chen − School of Architectural Intelligence, Jiangsu Vocational Institute of Architectural Technology, Xuzhou 221116, P. R. China

Xing-Shun Cong − College of Chemical Engineering, Zaozhuang University, Zaozhuang 277160, P. R. China

Complete contact information is available at:
https://pubs.acs.org/10.1021/acsomega.2c03846

Notes

The authors declare no competing financial interest.

REFERENCES

(1) Wang, H.; Zhang, L.; Chen, Z.; Hu, J.; Li, S.; Wang, Z.; Liu, J.; Wang, X. Semiconductor heterojunction photocatalysts: design, construction, and photocatalytic performances. *Chem. Soc. Rev.* **2014**, *43*, No. 5234.

(2) Jayaraman, T.; Murthy, A. P.; Elakkiya, V.; Chandrasekaran, S.; Nithyadharseni, P.; Khan, Z.; Senthil, R. A.; Shanker, R.; Raghavender, M.; Kuppusami, P.; Madhavan, J.; Ashokkumar, M. Recent development on carbon based heterostructures for their applications in energy and environment: A review. *J. Ind. Eng. Chem.* **2018**, *64*, 16−59.

(3) Renou, S.; Givaudan, J. G.; Poulain, S.; Dirassouyan, F.; Moulin, P. Landfill leachate treatment: review and opportunity. *J. Hazard. Mater.* **2008**, *150*, 468−493.

(4) Li, Y.; Geng, Z.; Yang, S.; Wang, Z.; Chen, T.; Yu, X.; Guo, Q.; Rong, H.; Duan, T.; Zhu, W. Integration of bio-inspired adsorption and photodegradation for the treatment of organics-containing radioactive wastewater. *Chem. Eng. J.* **2019**, *364*, 139−145.

(5) Zhang, S.; Li, B.; Wang, X.; Zhao, G.; Hu, B.; Lu, Z.; Wen, T.; Chen, J.; Wang, X. Recent developments of two dimensional graphene-based composites in visible-light photocatalysis for eliminating persistent organic pollutants from wastewater. *Chem. Eng. J.* **2020**, *390*, No. 124642.

(6) Katheresan, V.; Kansedo, J.; Lau, S. Y. Efficiency of various recent wastewater dye removal methods: a review. *J. Environ. Chem. Eng.* **2018**, *6*, 4676−4697.

(7) Kong, Z.; Li, L.; Xue, Y.; Yang, M.; Li, Y. Y. Challenges and prospects for the anaerobic treatment of chemical-industrial organic wastewater: a review. *J. Cleaner Prod.* **2019**, *231*, 913−927.

(8) Wang, W. L.; Cai, Y. Z.; Hu, H. Y.; Chen, J.; Wang, J.; Xue, G.; Wu, Q. Y. Advanced treatment of bio-treated dyeing and finishing wastewater using ozone-biological activated carbon: a study on the synergistic effects. *Chem. Eng. J.* **2019**, *359*, 168−175.

(9) Jun, B. M.; Heo, J.; Taheri-Qazvini, N.; Park, C. M.; Yoon, Y. Adsorption of selected dyes on $Ti_3C_2T_x$ MXene and Al-based metal-organic framework. *Ceram. Int.* **2020**, *46*, 2960−2968.

(10) Yang, T.; Peng, J.; Zheng, Y.; He, X.; Hou, Y.; Wu, L.; Fu, X. Enhanced photocatalytic ozonation degradation of organic pollutants by ZnO modified TiO_2 nanocomposites. *Appl. Catal., B* **2018**, *221*, 223−234.

(11) Litter, M. I. Review Heterogeneous photocatalysis transition metal ions in photocatalytic systems. *Water Res.* **2010**, *44*, No. 5511.

(12) Lin, Y.; Li, D.; Hu, J.; Xiao, G.; Wang, J.; Li, W.; Fu, X. Highly efficient photocatalytic degradation of organic pollutants by PANI-modified TiO_2 composite. *J. Phys. Chem. C* **2012**, *116*, 5764−5772.

(13) Kisch, H. Semiconductor photocatalysis-mechanistic and synthetic aspects. *Angew. Chem., Int. Ed.* **2013**, *52*, 812−847.

(14) Verma, N.; Ananthakrishnan, R. Riboflavin-immobilized CeO_2−RGO nanohybrid as a potential photoredox catalyst for enhanced removal of organic pollutants under visible light. *J. Phys. Chem. C* **2020**, *124*, 404−415.

(15) Chong, M. N.; Jin, B.; Chow, C. W.; Saint, C. Recent developments in photocatalytic water treatment technology: a review. *Water Res.* **2010**, *44*, 2997−3027.

(16) Sha, Z.; Chan, H. S.; Wu, J. Ag_2CO_3/UiO-66(Zr) composite with enhanced visible-light promoted photocatalytic activity for dye degradation. *J. Hazard. Mater.* **2015**, *299*, 132−140.

(17) Lin, H.; Maggard, P. A. Synthesis and structures of a new series of silver-vanadate hybrid solids and their optical and photocatalytic properties. *Inorg. Chem.* **2008**, *47*, 8044−8052.

(18) Gao, C.; Chen, S.; Wang, Y.; Wang, J. W.; Zheng, X. S.; Zhu, J.; Song, F.; Zhang, L.; Xiong, W. K.; Heterogeneous, Y. J. single-atom catalyst for visible-light-driven high-turnover CO_2 reduction: The role of electron transfer. *Adv. Mater.* **2018**, *30*, No. 1704624.

(19) Sun, X.; Habibul, N.; Du, H. Co0.85Se magnetic nanoparticles supported on carbon nanotubes as catalyst for hydrogen evolution reaction. *Chin. J. Catal.* **2021**, *42*, 235−243.

(20) Bie, C. B.; Yu, H. G.; Cheng, B.; Ho, W.; Fan, J. J.; Yu, J. G. Design, fabrication, and mechanism of nitrogen-doped graphene-based photocatalyst. *Adv. Mater.* **2021**, *33*, No. 2003521.

(21) Peng, W.; Yang, X. X.; Mao, L. C.; Jin, J. H.; Yang, S. L.; Zhang, J. J.; Li, G. ZIF-67-derived Co nanoparticles anchored in N doped hollow carbon nanofibers as bifunctional oxygen electrocatalysts. *Chem. Eng. J.* **2021**, *407*, No. 127157.

(22) Moon, H. R.; Lim, D. W.; Suh, M. P. Fabrication ofmetal nanoparticles in metal-organic frameworks. *Chem. Soc. Rev.* **2013**, *42*, 1807−1824.

(23) Kim, T. K.; Lee, K. J.; Cheon, J. Y.; Lee, J. H.; Joo, S. H.; Moon, H. R. Nanoporous metal oxides with tunable and nanocrystalline frameworks via conversion of metal-organic frameworks. *J. Am. Chem. Soc.* **2013**, *135*, 8940−8946.

(24) Sun, J. K.; Xu, Q. Functional materials derived from open framework templates/precursors: synthesis and applications. *Energy Environ. Sci.* **2014**, *7*, No. 2071.

(25) Xiao, J. D.; Jiang, H. L. Metal-organic frameworks for photocatalysis and photothermal catalysis. *Acc. Chem. Res.* **2019**, *52*, 356−366.

(26) Hamon, L.; Serre, C.; Devic, T.; Loiseau, T.; et al. Comparative study of hydrogen sulfide adsorption in the MIL-53(Al, Cr, Fe), MIL-47(V), MIL-100(Cr), and MIL-101(Cr) metal-organic frameworks at room temperature. *J. Am. Chem. Soc.* **2009**, *131*, 8775−8777.

(27) Lee, J.; Farha, O. K.; Roberts, J.; Scheidt, K. A.; Nguyen, S. T.; Hupp, J. T. Metal-organic framework materials as catalysts. *Chem. Soc. Rev.* **2009**, *38*, No. 1450.

(28) Huang, W. Y.; Liu, N.; Zhang, X. D.; Wu, M. H.; Tang, L. Metal organic framework g-C_3N_4/MIL-53(Fe) heterojunctions with enhanced photocatalytic activity for Cr(VI) reduction under visible light. *Appl. Surf. Sci.* **2017**, *425*, 107−116.

(29) Wang, L.; Wan, J.; Zhao, Y.; Yang, N.; Wang, D. Hollow multi-shelled structures of Co_3O_4 dodecahedron with unique crystal orientation for enhanced photocatalytic CO_2 reduction. *J. Am. Chem. Soc.* **2019**, *141*, 2238−2241.

(30) Wu, J.; Wang, S.; Lei, Z.; Guan, R.; Chen, M.; Wu, P.; Lu, Y.; Cao, R.; Yang, S. Pomegranate-like C-60@cobalt/nitrogen-codoped porous carbon for high-performance oxygen reduction reaction and lithium-sulfur battery. *Nano. Res.* **2021**, *14*, 2596−2605.

(31) Zhong, W.; Liu, H.; Bai, C.; Liao, S.; Li, Y. Base-free oxidation of alcohols to esters at room temperature and atmospheric conditions using nanoscale Co-based catalysts. *ACS Catal.* **2015**, *5*, 1850−1856.

(32) Li, J.; Xia, W.; Tang, J.; Tan, H.; Wang, J.; Kaneti, Y.; Bando, Y.; Wang, T.; He, J.; Yamauchi, Y. MOF nanoleaves as new sacrificial templates for the fabrication of nanoporous Co-N x/C electrocatalysts for oxygen reduction. *Nanoscale Horiz.* **2019**, *4*, 1006−1013.

(33) Chen, Z.; Wu, R.; Liu, Y.; Ha, Y.; Guo, Y.; Sun, D.; Liu, M.; Fang, F. Ultrafine Co nanoparticles encapsulated in carbon-nano-tubes-grafted graphene sheets as advanced electrocatalysts for the hydrogen evolution reaction. *Adv. Mater.* **2018**, *30*, No. 1802011.

(34) Xu, Y.; Tu, W.; Zhang, B.; Yin, S.; Huang, Y.; Kraft, M.; Xu, R. Nickel nanoparticles encapsulated in fewlayer nitrogen-doped graphene derived from metal-organic frameworks as efficient bifunctional electrocatalysts for overall water splitting. *Adv. Mater.* **2017**, *29*, No. 1605957.

(35) Zhang, H.; Wang, T.; Wang, J.; Liu, H.; Dao, T.; Li, M.; Liu, G.; Meng, X.; Chang, K.; Shi, L.; Nagao, T.; Ye, J. Surface-plasmon-enhanced photodriven CO_2 reduction catalyzed by metal-organic-framework-derived iron nanoparticles encapsulated by ultrathin carbon layers. *Adv. Mater.* **2016**, *28*, 3703−3710.

(36) Zhang, M.; Dai, Q.; Zheng, H.; Chen, M.; Dai, L. Novel MOF-derived Co@N-C bifunctional catalysts for highly efficient Zn-air batteries and water splitting. *Adv. Mater.* **2018**, *30*, No. 1705431.

(37) Tian, H.; Zhang, C.; Su, P.; Shen, Z.; Liu; Wang, H. G.; Liu, S.; Liu, J. Metal-organic-framework-derived formation of Co-N-doped carbon materials for efficient oxygen reduction reaction. *J. Energy Chem.* **2020**, *40*, 137−143.

(38) Guo, J.; Zhang, Y.; He, Y. C.; Shan, J. Photocatalytic performance of Co_3O_4/C based on ZIF-67/C composite materials. *Polyhedron* **2020**, *175*, No. 114215.

(39) Yang, S. J.; Im, J. H.; Kim, T.; Lee, K.; Park, C. R. MOF-derived ZnO and ZnO@C composites with high photocatalytic activity and adsorption capacity. *J. Hazard. Mater.* **2011**, *186*, 376−382.

(40) Xia, Y.; Chen, B.; Zhu, Y.; Kong, D.; Gui, P. Atomically homogeneous dispersed ZnO/N-doped nanoporous carbon compo-sites with enhanced CO_2 uptake capacities and high efficient organic pollutants removal from water. *Carbon* **2015**, *95*, 113−124.

(41) Hussain, M. Z.; Schneemann, A.; Fischer, R. A.; Zhu, Y.; Xia, Y. MOF derived porous ZnO/C nanocomposites for efficient dye photodegradation. *ACS Appl. Energy Mater.* **2018**, *1*, 4695−4707.

(42) Qian, J.; Sun, F.; Qin, L. Hydrothermal synthesis of zeolitic imidazolate framework-67 (ZIF-67) nanocrystals. *Mater. Lett.* **2012**, *82*, 220−223.

(43) Das, R.; Pachfule, P.; Banerjee, R.; Poddar, P. Metal and metal oxide nanoparticle synthesis from metal organic frameworks (MOFs): finding the border of metal and metal oxides. *Nano* **2012**, *4*, 591−599.

(44) Zhang, F.; Yuan, C.; Zhu, J.; Wang, J.; Zhang, X.; Lou, X. Flexible films derived from electrospun carbon nanofibers incorpo-rated with Co_3O_4 hollow nanoparticles as self-supported electrodes for electrochemical capacitors. *Adv. Funct. Mater.* **2013**, *23*, 3909−3915.

(45) Ouyang, T.; Cheng, K.; Gao, Y.; Kong, S.; Ye, K.; Wang, G.; Cao, D. Molten salt synthesis of nitrogen doped porous carbon: a new preparation methodology for highvolumetric capacitance electrode materials. *J. Mater. Chem. A* **2016**, *4*, 9832−9843.

(46) Barreca, D.; Massignan, C.; Daolio, S.; Fabrizio, M.; Piccirillo, C.; Armelao, L.; Tondello, E. Composition and microstructure of cobalt oxide thin films obtained from a novel cobalt(II) precursor by chemical vapor deposition. *Chem. Mater.* **2001**, *13*, 588−593.

(47) Collinge, G.; Xiang, Y. Z.; Barbosa, R.; McEwen, J. S.; Kruse, N. CO-induced inversion of the layer sequence of a model CoCu catalyst. *Surf. Sci.* **2016**, *648*, 74−83.

(48) Wang, Z.; Peng, S.; Hu, Y.; Li, L.; Yan, T.; Yang, G.; Ji, D.; Srinivasan, M.; Pan, Z.; Ramakrishna, S. Cobalt nanoparticles encapsulated in carbon nanotube-grafted nitrogen and sulfur co-doped multichannel carbon fibers as efficient bifunctional oxygen electrocatalysts. *J. Mater. Chem. A* **2017**, *5*, 4949−4961.

(49) Xue, Y.; Liu, J.; Chen, H.; Wang, R.; Li, D.; Qu, J.; Dai, L. Nitrogen-doped graphene foams as metal-free counter electrodes in high-performance dye-sensitized solar cells. *Angew. Chem., Int. Ed.* **2012**, *51*, 12124−12127.

(50) Chen, L.; Xu, C.; Du, R.; Mao, Y.; Xue, C.; Chen, L.; Qu, L.; Zhang, J.; Yi, T. Rational design of three-dimensional nitrogen-doped carbon nanoleaf networks for high performance oxygen reduction. *J. Mater. Chem. A* **2015**, *3*, 5617−5627.

(51) Wang, S.; Guan, B. Y.; Lou, X. W. Rationally designed hierarchical N-doped carbon@$NiCo_2O_4$ double-shelled nanoboxes for enhanced visible light CO_2 reduction. *Energy Environ. Sci.* **2018**, *11*, 306−310.

(52) Xie, X.; Su, D.; Zhang, J.; Chen, S.; Mondal, A. K.; Wang, G. A comparative investigation on the effects of nitrogen-doping into graphene on enhancing the electrochemical performance of SnO_2/graphene for sodium-ion batteries. *Nanoscale* **2015**, *7*, 3164−3172.

(53) Nosaka, Y.; Nosaka, A. Y. Generation and detection of reactive oxygen species in photocatalysis. *Chem. Rev.* **2017**, *117*, 11302−11336.

■ NOTE ADDED AFTER ASAP PUBLICATION

This paper was published ASAP on October 26, 2022, with errors in the TOC graphic and Figure 2. The corrected version was reposted on October 27, 2022.